



A practical fabrication strategy for wire arc additive manufacturing of metallic parts with wire structures

Ziping Yu¹ · Zengxi Pan¹ · Donghong Ding² · Joseph Polden¹ · Fengyang He¹ · Lei Yuan¹ · Huijun Li¹

Received: 9 February 2021 / Accepted: 28 May 2021 / Published online: 5 June 2021

© The Author(s), under exclusive licence to Springer-Verlag London Ltd., part of Springer Nature 2021

Abstract

Wire arc additive manufacturing (WAAM) is well suited for the manufacture of sizeable metallic workpieces featuring medium-to-high geometrical complexity due to its high deposition rate, low processing conditions limit, and environmental friendliness. To enhance the current capability of the WAAM process for fabricating structures with complex geometry, this paper proposes a robot-based WAAM strategy adapted specifically for fabricating freeform parts with wire structures composed of multiple struts. Contributions in this work include: (i) The study of bead modelling, which establishes optimal welding parameter selection for the process; (ii) the novel manufacturing strategy, including the adaptive slicing methodology and height control system for accurately depositing every single strut; and (iii) detailed manufacturing procedures for multi-strut branch intersections as well as the collision-free path planning to control the overall fabrication process. To verify the effectiveness of this proposed WAAM approach, two complex wire structures were fabricated successfully, indicating the feasibility of the proposed fabrication strategy.

Keywords Additive manufacturing · Gas metal arc welding · Wire structures · Freeform fabrication

1 Introduction

Wire arc additive manufacturing (WAAM) is an emerging directed energy deposition (DED) additive manufacturing technology [1] that utilizes electric arc as the power source, which can provide high heat input and deposition rates. Due to its rapid prototyping capability [2] and simplistic equipment setup [3, 4], it becomes a promising alternative to manufacture large metallic components with medium-to-high geometrical complexity [5], particularly in aerospace, automotive, and rapid tooling industries [6]. Recent studies also show practical applications of this process in the field of construction. Kloft et al. [7] proposed a novel strategy for producing the reinforced concrete elements in combined additive

manufacturing. Gardner et al. [8] proposed the systematic safety verification method for additively manufactured large-scale metal structures. On this basis, Laghi et al. [9] conducted a detailed study on the properties of the WAAM-produced material and calibrated its mechanical properties and partial safety factors, which further improved the practicability of WAAM processing.

In recent years, WAAM has been integrated with industrial robotic systems or computer-aided manufacturing (CAM) systems, allowing it to perform multi-axis freeform deposition in three-dimensional space [10] such as wire structures fabricated in ref [11]. Wire structures are skeleton-like components composed of many interconnected support struts. Initially, this type of structure has been widely employed in polymer AM. Huang et al. [12] pointed out that wire structures can reduce material requirements and costs if adequately integrated into a given parts' design. Mueller et al. [13] stated that this structure could reduce the mass of a given component while maintaining its structural stability, thereby increasing the efficiency of the fabricating process. Similarly, for metallic wire structures, several attempts have been made to illustrate that using metal wire structures to replace thin-walled or solid structures enables weight reduction while maintaining high strength also [14]. Moreover, the MX3D team carried out many high-

✉ Zengxi Pan
zengxi@uow.edu.au

¹ School of Mechanical, Materials & Mechatronic, Faculty of Engineering and Information Sciences, University of Wollongong, Northfield Ave, Wollongong, NSW 2500, Australia

² School of Mechatronic Engineering and Automation, Foshan University, Foshan 528225, Guangdong, China

profile projects that emphasize the unique artistic and practical values of these metal wire structures. Laghi et al. [15] also demonstrated that WAAM has the potential to change the current design and manufacturing methods of steel structures via exhibiting the large-scale WAAM-produced diagrid column to the public.

A significant difference between the fabrication of wire structures and others (such as thin-walled or solid structures) is that the material is successively added in a point-by-point manner [11] instead of continuous bead deposition layer-by-layer [16]. Therefore, to successfully implement WAAM for producing wire structures, an accurate point-by-point bead model is required to predict and control the forming shape of each deposition and, ultimately, the geometry of the final part [17].

The adaptive slicing algorithm and multi-directional path planning method are also essential for the freeform fabrication of wire structures. Yuan et al. [18] have implemented a multi-directional deposition method for fabricating overhang parts without using any supports. Non-layerwise slicing methods are widely developed in AM of complex structures [19]. For the deposition strategy of the wire structures, Radel et al. [11] reported that struts could be fabricated through depositing material point-by-point in space with acceptable fabrication efficiency.

In producing wire structures, the welding torch may have a greater collision probability due to the complexity of parts. Wu et al. [20] changed the orientation of the extrusion head to avoid the collision. However, in the WAAM of wire structures, the orientation of the welding torch is limited due to the characteristics of the welding process.

In this paper, a number of essential strategies for manufacturing metallic wire structures using the point-to-point WAAM process, from bead modelling to the final torch-based deposition path planning, were proposed. The developed methods aim to reduce processing difficulty and improve the overall efficiency in manufacturing these wire structures. The contributions here are demonstrated by fabricating two different parts with wire structures via the proposed methodology.

2 Problem definitions

2.1 Wire structure definition

The parts with wire structures consist of a network of interconnected struts. Each strut is built up by a series of successive deposits formed by point-by-point welding, and each point is welded for a certain time, during which the torch remains stationary. Subsequently, the torch is moved up along the strut build direction [21]. The projected shape of the deposits is similar to a hemisphere,

as summarized by Abe et al. [22]. Its characteristic geometric parameters can be defined by layer height increment (Δh) and layer diameter (d), as shown in Fig. 1. Due to overlapping between neighboring beads, as described by Ding et al. [23], height increment Δh of each layer is obtained by calculating the difference between the height of the next layer and the current layer, which is expressed as:

$$\Delta h_n = h_n - h_{n-1} \quad (1)$$

where n represents the number-of-time welding; this clarifies that the welding position of each layer is the same as the previous layer height coordinates. To highlight this, each layer of a strut is denoted as L_n , whose coordinates are the same as h_n . Whenever L_n is mentioned, it also includes a Δh_n , which is used to find the next welding layer L_{n+1} .

In the fabrication process, each layer is considered to have the same material composition and thermal conductivity. Note that the material of the substrate and the filled wire may have a subtle difference leading the inaccuracies in the process during the deposition of the first few layers. Thus, strut-like substrates consisting of several layers need to be deposited before starting to fabricate wire structures.

Due to unavoidable interferences in the physical welding process, layers with abnormal shapes may occasionally appear, as shown in Fig. 1. For the experiments conducted in this work, these samples (which lie significantly outside of the average data range) will be excluded to reduce errors and improve the model accuracy.

2.2 Introduction to strut processing directions

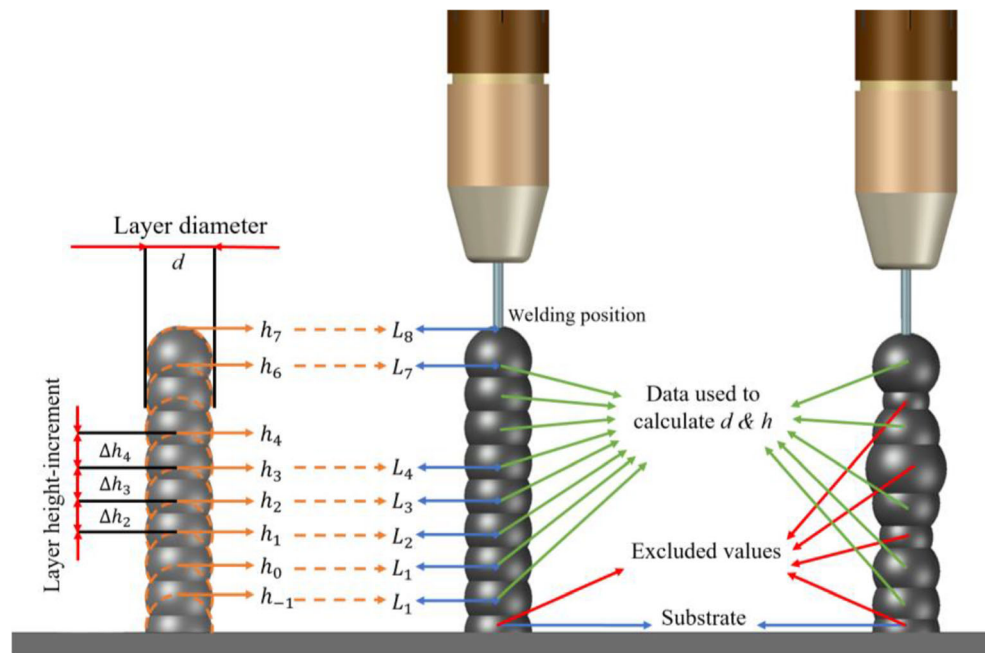
A schematic diagram describing the build direction and torch direction of a wire structure is shown in Fig. 2. During the deposition, the torch direction always remains parallel with the build direction of the strut. During each welding period, the torch remains stationary at a certain distance from the deposition point, referred to as the contact tip to work distance ($ctwd$). A strut with an inclined build direction will feature a certain slope k between the two layers L_m and L_n . The torch direction will also have an inclined angle α_m (relative to the ground), defined as:

$$\alpha_m = \tan^{-1} \frac{L_{nz} - L_{mz}}{L_{nx} - L_{mx}} = \tan^{-1} k_m \quad (2)$$

It is worth noting that for these non-vertical struts, Δh is not measured vertically upward along the z -axis direction but follows the build direction of the strut with the slope k_m .

The alteration point highlighted in Fig. 2 is used to distinguish when the build direction of the strut varied

Fig. 1 Definition of layer geometry, substrate, and layer data collected

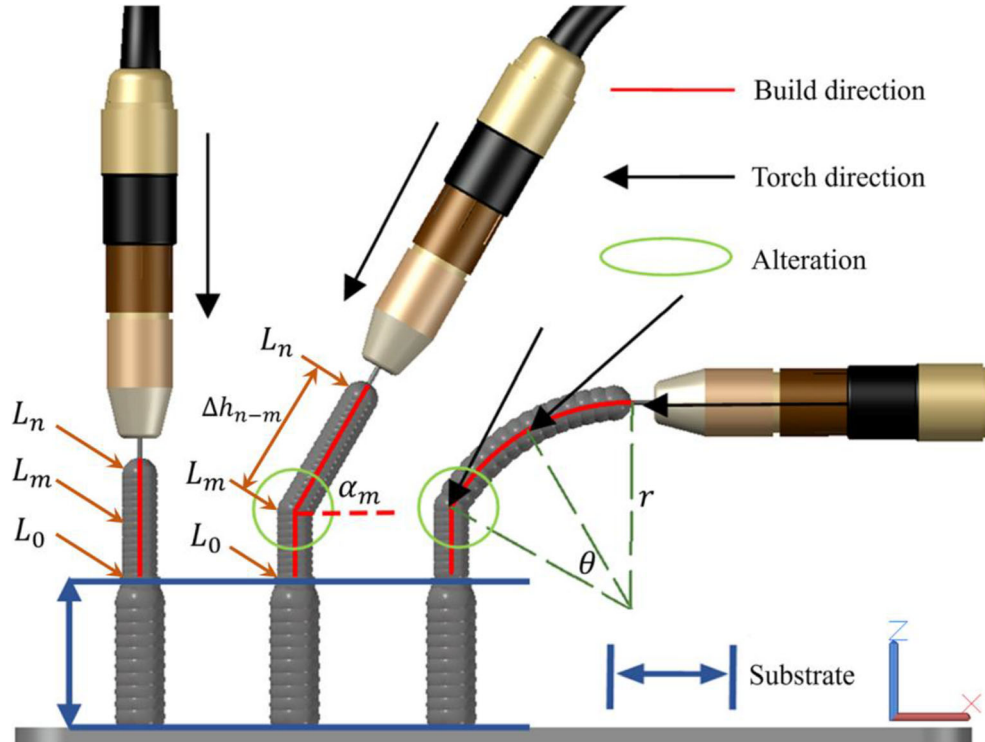


so that the torch can adjust its direction accordingly. In situations where the build direction changes smoothly with the Bezier curve, no alteration point is required. The geometric data required for these calculations can be readily obtained from CAD data. This point defined zones where an adaptive slicing process is required, which is detailed in the following sections.

3 Experimental setup

Experiments are carried out employing the robotic WAAM system, as shown in Fig. 3, which includes an ABB IRB2600, the Fronius welding system, and a workpiece positioner. The robotic WAAM system was controlled through an integrated computer-aided interface, presented

Fig. 2 The schematic of the build direction, torch direction of the single strut



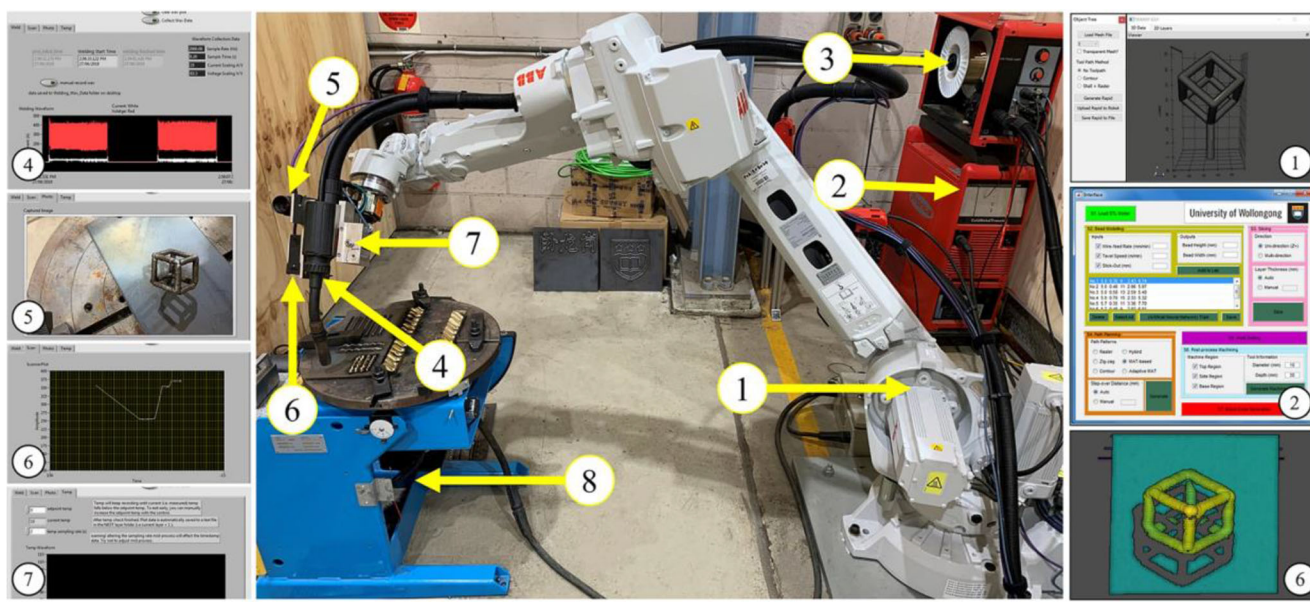


Fig. 3 WAAM system. (1) IRB 2600; (2) TransPuls Synergic 5000 CMT welder; (3) VR 7000 CMT wire feeder; (4) CMT torch; (5) CCD camera; (6) 3D profile scanner; (7) infrared temperature sensor; (8) 2-DOF workpiece positioner

previously in [17]. This software aimed to display arbitrary imported CAD models visually and obtain the desired workpiece geometry. It was designed to automatically slice the workpiece, calculate tool processing paths, and then directly generate the corresponding robot code and welding parameters for the manufacturing process.

A multi-functional tool was developed through integrating a CCD camera, a 3D profile scanner, and an infrared temperature sensor into a Fronius robacta drive CMT welding torch. The camera is used to capture the visual appearance of the workpiece during processing. A 3D profile scanner is used to obtain the geometric profile of deposited layers. And the infrared temperature sensor is implemented to monitor the inter-layer temperature of the welding process. The functions mentioned above, together with welding current and voltage acquisition functions, have been integrated into LabVIEW to establish a feedback control for improving the reliability and accuracy of the deposition process.

The filling wire was mild steel (ER70S-6) welding wire with a diameter of 0.9 mm. A shielding gas mixture of 15% CO₂ and 85% argon was employed with a flow rate of 15 L/min. The default *ctwd* used in the experiment is set to 9 mm to provide a relatively constant rate of gas shielding. The chemical composition and mechanical properties of the selected welding wire are listed in Table 1.

The cold metal transfer (CMT) welding process was adopted to reduce heat input during the welding process with high-quality results. This method is substantially suitable for welding thin-walled structures with small widths [24]. Moreover, according to recent research results by Müller et al. [21], the CMT welding process can make the strut have a better geometry, smaller and rarer pores, and a more even

strain distribution compared to the traditional GMAW welding process.

4 Implementation and discussion

The core contributions of this paper are presented here, which spread over four key areas: the bead modelling, a height control system, an adaptive slicing methodology, and finally, the tool path planning strategies that combine these techniques to produce an efficient means of fabricating complex wire structures.

4.1 Strut-based bead modelling

Process parameters have significant effects on the forming quality of the strut. Therefore, it is critical to establish a

Table 1 Chemical composition and properties of ER70S-6

Chemical composition of ER70S-6 mild steel wire (wt.%)

Composition	Mn	Si	Cu	C	S	P
ER70S-6 Wire	1.53	0.88	0.18	0.08	0.01	0.009
Some properties of steel ER70S-6 in specshield 15% CO ₂ , Ar						
Melt temperature (T)				1700K		
Density (ρ)				6500 kg/m ³		
Surface tension (γ)				1.3 N/m		
Tensile strength				85–90,000 psi		
Yield strength				7–75,000 psi		

strut-based bead model to determine the appropriate parameters for producing a geometrically accurate part. In this experiment, the welding arc-on time (wt) and wire feeding speed (wfs) are the major welding process parameters that dominate the strut geometry. Across all tests, the inter-layer temperature is cooled down to around room temperature so as to ensure that each layer has the same heat condition. The $ctwd$ used in this part is also calibrated to the default value of 9 mm during each layer depositing process.

Experiments are conducted for four different wfs (from 4 to 7 m/min) at four different wt (from 1.5 to 3 s), as shown in Table 2. Substrates with ten layers were first deposited with $v = 9$ m/min and $t=3$ s before the strut welding process began to eliminate the interference of external factors in the first few layers of struts. Each deposited strut consists of 20 layers, and two struts with the same set of process parameters were fabricated, so a total of 40 sets of data were obtained under each parameter combination. The 3D profile scanner is used to obtain the height and diameter data of a strut. It uses the average value of the z -coordinates near the deposition center as the height of the current layer and takes the largest difference between the scan edge points (x, y) as the diameter of the current layer. After collecting all the data of the strut layers, the average value of these data will be taken as the final measurement value, including the diameter and the layer height increment of the current strut.

Figure 4 illustrates the effect of (a) wfs and (b) wt on the layer geometry. The graphs indicate a linear correlation between them, and the change in Δh_m is more closely related to the value of wt . Based on this, a non-linear regression equation is computed to correlate the resultant strut geometries relative

to the wfs and wt , as shown in Fig. 4 (c). Their expressions were defined as:

$$V = C_{00} + C_{10}w + C_{01}t + C_{20}w^2 + C_{11}wt + C_{02}t^2 \quad (3)$$

where if the response V represents h , $C_{00}=0.479$, $C_{10}=0.065$, $C_{01}=0.45$, $C_{20}=-0.001$, $C_{11}=-0.01$, $C_{02}=-0.0325$; else if V represents d , $C_{00}=3.94$, $C_{10}=-0.282$, $C_{01}=0.832$, $C_{20}=0.04$, $C_{11}=0.153$, $C_{02}=-0.1126$.

Table 2 lists the fitting results d_p and Δh_p , with the corresponding error, which is defined as the percentage deviation between the fitting value and the measured geometry, calculated by:

$$E_w = \frac{|e_p - e_m|}{e_m} \times 100\% \quad (4)$$

where e represents d and h respectively.

The normalized analysis is provided to compare the variation between measured values and predicted data, as shown in Fig. 5. All data is firstly normalized to X_i , which is determined by:

$$X_i = \frac{2}{R_{max} - R_{min}} (R_i - R_{min}) - 1 \quad (5)$$

where R_{max} and R_{min} are the max and min data of the raw actual measured data. The solid orange line ($y = x$) shown in Fig. 5 indicates that the measured values closely match their predicted counterpart. In this figure, most of the points are located on or near the line, which indicates that the proposed

Table 2 Process parameters and layer geometry formation

No	Process parameter	Measured results		Fitting results		E_d (mm)	E_h (mm)
		wt (s)	wfs (m/min)	d_m (mm)	Δh_m (mm)		
1	1.5	4.0		5.37	1.27	5.363	1.272
2	2.0	4.0		5.90	1.42	5.889	1.420
3	2.5	4.0		6.30	1.55	6.358	1.552
4	3.0	4.0		6.72	1.67	6.771	1.668
5	1.5	5.0		5.74	1.32	5.668	1.317
6	2.0	5.0		6.34	1.48	6.270	1.460
7	2.5	5.0		7.02	1.56	6.816	1.587
8	3.0	5.0		7.31	1.71	7.306	1.698
9	1.5	6.0		5.94	1.36	6.052	1.360
10	2.0	6.0		6.66	1.49	6.731	1.499
11	2.5	6.0		7.26	1.62	7.354	1.621
12	3.0	6.0		7.88	1.73	7.920	1.727
13	1.5	7.0		6.23	1.40	6.515	1.403
14	2.0	7.0		7.37	1.53	7.270	1.536
15	2.5	7.0		7.69	1.68	7.970	1.654
16	3.0	7.0		8.71	1.74	8.613	1.755

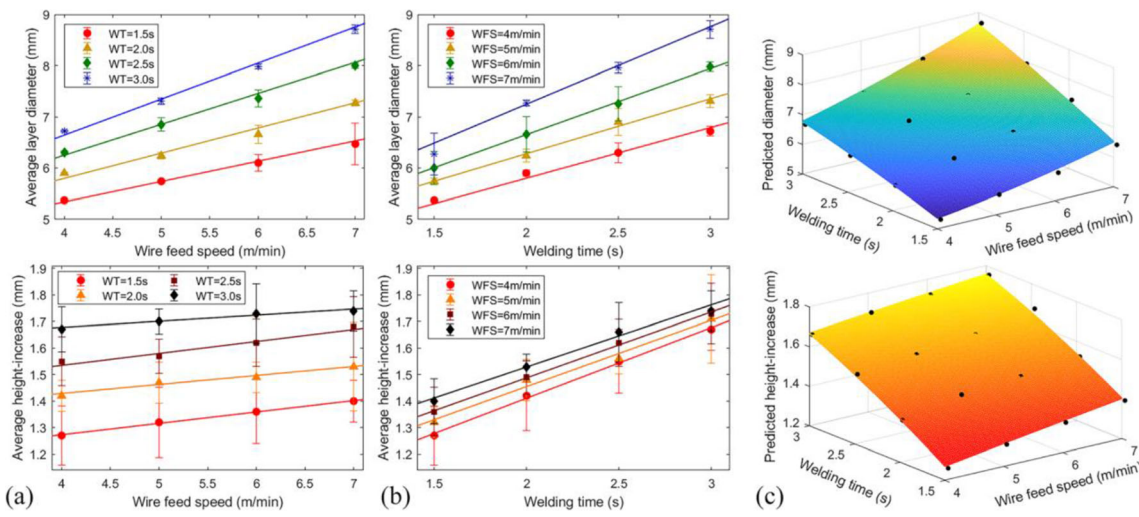


Fig. 4 The effect of (a) WFS, (b) WT on the layer geometry, and (c) fitting result

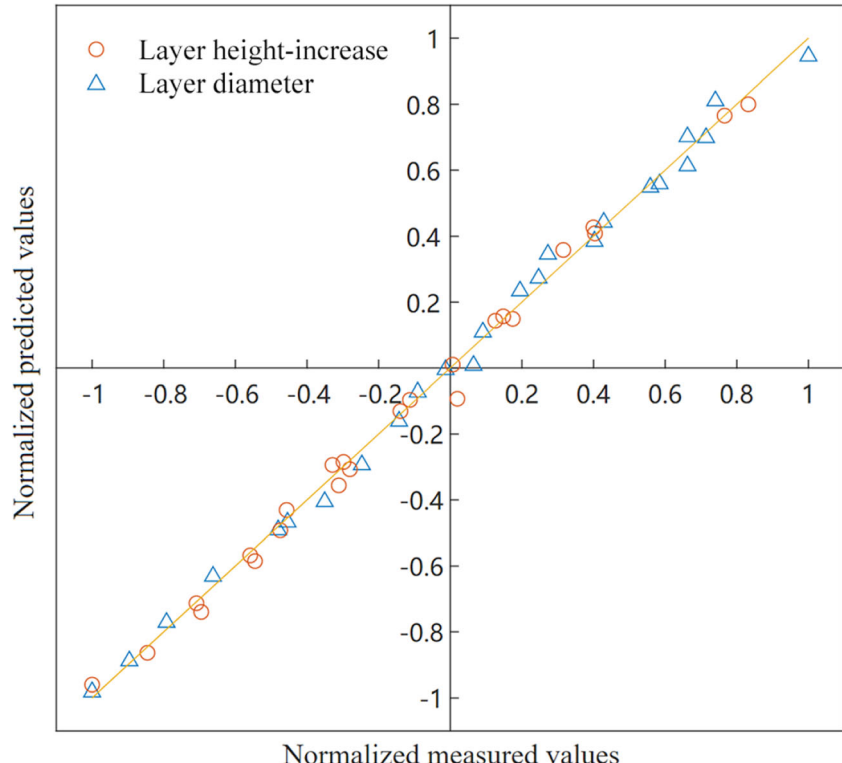
bead modelling is able to accurately predict the layer geometry of a well-formed strut within a given range.

Except for bead modelling established for vertical-down deposition, it must also ascertain layer geometry formation when the strut has an inclined angle. In WAAM, the surface tension of the welding pool acts to counter gravitational forces during the welding process. For each deposit, the Eotvos number E_o reported in [11] is used to represent the effect of gravity relative to surface tension, which is expressed as:

$$Eo = \frac{\Delta\rho g L^2}{4\gamma} \quad (6)$$

where γ and $\Delta\rho$ are obtained from Table 1. L is defined as the characteristic length. Here, it is considered as the layer diameter d . As a general rule, when $Eo < 1$ (that is, $d < 9$ mm), the molten pool can be maintained at the required position predominantly supported by the surface tension [11]. Therefore, it is concluded that the deposition process can be

Fig. 5 Comparison between predicted and measured value (normalized)



carried out at an arbitrary angle under all the process parameter combinations studied in the proposed bead modelling. For struts with different angles, their layer geometries are only related to the welding parameters wfs and wt , but not the inclined angle. Figure 6 demonstrates these findings, where a number of struts were deposited with a strut angle varying from 0 to 60 degrees concerning the vertical position as the regular one.

4.2 Height control system

As shown in Fig. 4 (b), there are variations ($\pm 20\%$) between the predicted value of the layer height increment and the actual measured values. Therefore, as the fabrication process continues, differences between the predicted layer height increment and actual deposited layer height can occasionally occur to lead to cumulative errors. This can severely deteriorate the overall geometry of the deposited part.

To overcome this challenge, the paper proposes an alternative method using lag control to adjust the welding point when the actual height increment of a layer does not match the theoretical one, in which the $ctwd$ (c) is used as the study object to find their difference. When there is a difference between the actual height Δh_a and the theoretical height increment Δh , if the torch is still moving Δh_a along the build direction, the $ctwd$ on this layer will change.

Yuan et al. [25] pointed out that the change of $ctwd$ can be reflected by the change of welding voltage. To do this, a number of tests were conducted, where the test range of c is from 4 to 24 mm, during which wfs is maintained at 4 m/min and wt at 2 s. The acquisition value of current and voltage is the average value, and the sampling frequency is 2000 Hz. The results are presented in Fig. 7. The current remains

relatively constant at 60 A, and the voltage has a positive linear correlation with the change of c . The actual Δh_a can be calculated by the difference between the c used in the bead modelling and the actual c_a shown by the voltage. It is worth mentioning that this method records the relationship between c and voltage, so it always assumes that the height increment of the current deposit layer is Δh .

When the deposition process of a layer is completed, the welding torch will shift the distance Δh to the next layer, regardless of the real height increment of the current layer. Then, during the processing phase for the next layer, if the recorded voltage V_a is different from the corresponding value for c , the position is then adjusted accordingly.

4.3 Adaptive slicing methodology

Combined with the height control system, an adaptive slicing algorithm is proposed to find the deposition points for each strut part. The first step is to extract the centroidal axes (or skeleton) of the complete wire structure. This will reduce the volumetric nature of the part to a more simplistic representation of points and lines. Next, we have the task of determining (a) the total number of individual struts s_i in the part and (b) the total number of layers $L_{i,n}$ contained in each of these struts.

Each strut in the part is defined by two feature points: namely, the start point n_{i1} and the end point n_{i2} . So, the strut is expressed as $s_i = [n_{i1}, n_{i2}]$. For any particular strut, no matter how complex its direction of growth, if it shares its start point n_{i1} with the end point of a different strut n_{j2} and its end point n_{i2} is shared with a start point of a different strut n_{j1} , then, the strut between these two characteristic points can be defined as an independent strut, as an example shown in Fig. 8 (b).

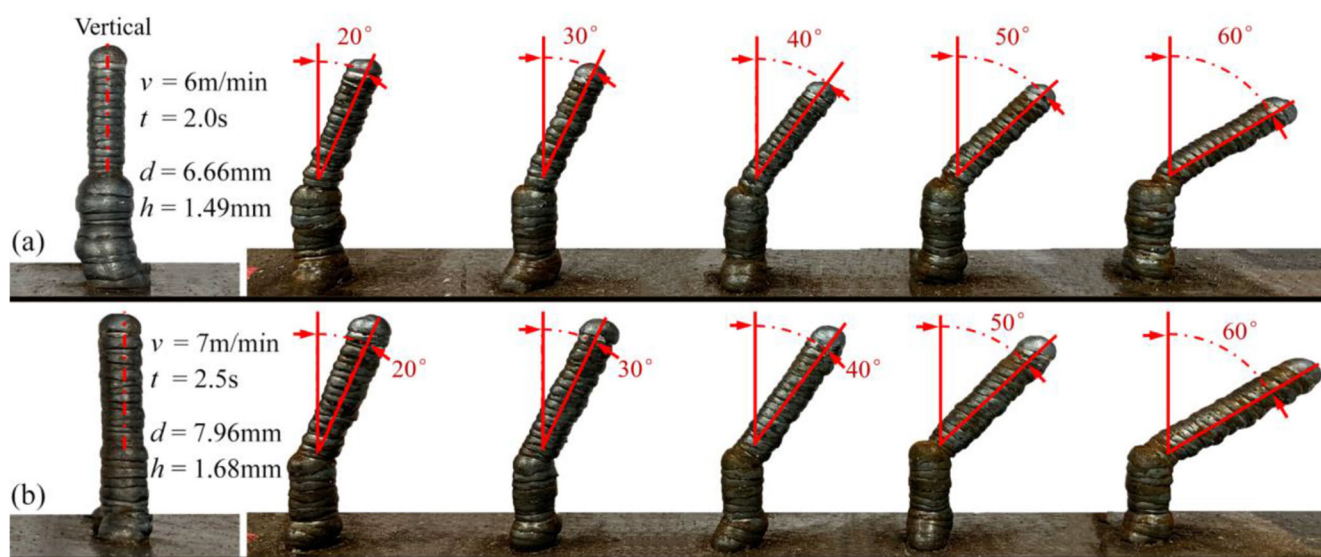
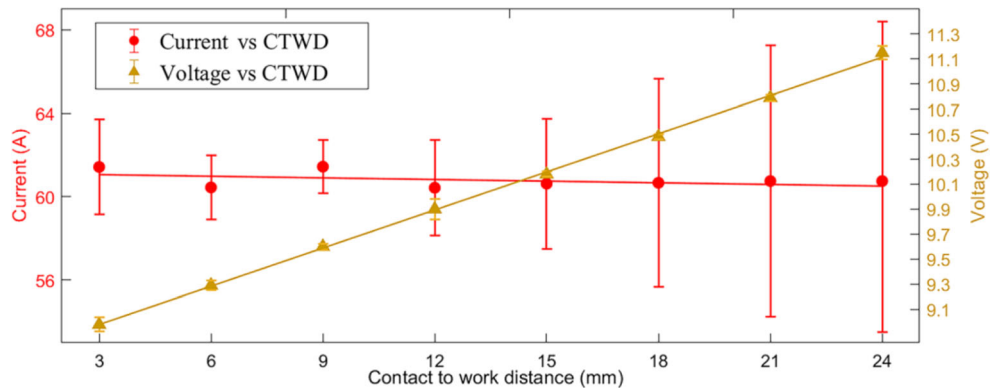


Fig. 6 The appearance of struts with inclined angles from 0° to 60° under the process parameter combination (a) $v = 6 \text{ m/min}$, $t = 2 \text{ s}$, and (b) $v = 7 \text{ m/min}$, $t = 2.5 \text{ s}$

Fig. 7 Relationship between the CTWD with the current and voltage, here $V_i = 0.1017c + 8.673$



After the classification of the individual struts is complete, the next step is to determine the number of layers $L_{i,n}$ belonging to each strut s_i . A simplistic approach, which splits the central axis of each strut into linear segments of length Δh , may seem logical but ultimately will not suffice in cases where the build direction of the strut changes. This approach will not accurately capture the actual height increment added during the deposition process. To overcome this, a different approach is proposed, as outlined in Fig. 8 (c). In this method, a sphere $C_{i,0}$ with a radius of Δh is used to slice each strut. The sphere is centered at the starting point of the first strut $L_{0,0}$, and the intersection of the sphere and s_0 is then used to define the deposition point of the next layer $L_{i,1}$. This process continues until all struts are processed. The deposition points for each layer $L_{i,n+1}$ are determined by the intersection of the sphere surface produced by the previous layer $L_{i,n}$. The coordinates for the point in the strut s_i can be defined as:

$$L_{i,n+1,x,y,z} = C_{i,n} \cap S - L_{i,n-1,x,y,z} \quad (7)$$

where $C_{i,n}$ is a sphere with its center at $L_{i,n}$ and a radius of Δh and S is a set containing all coordinates of s_i . However, the calculation for solving the intersection points of a sphere and

the build path of the strut is complicated and time-consuming. Therefore, this method can be optimized to find two points p_1 , p_2 on the strut whose distance R is equal to the slice length Δh , via:

$$\|R\| = \sqrt{\sum_{k=1}^N |L_{i,p1} - L_{i,p2}|^2} = \Delta h \quad (8)$$

where $L_{i,p}$ is a point on the strut with N elements; that is, the obtained point is the position of the slice layer. The first point $L_{i,p1}$ in this calculation is the start point $n_{i,1}$, and the next point $L_{i,p2}$ can be determined by finding a point Δh away from it along the build direction of the strut, and so on, until the entire strut is traversed. The algorithm divides a strut s_i into polylines of n layers with equal length. It is worth noting that the strut may not be divided exactly into n layers. In these situations, if the distance between the last slice layer and the end point $n_{i,2}$ of the strut is greater than Δh , then, an additional slice layer is added to the end point and vice versa.

Figure 9 discusses the performance of the slicing algorithm in some rare cases. If the curvature of the build direction of a strut changes significantly in a small range, its original path

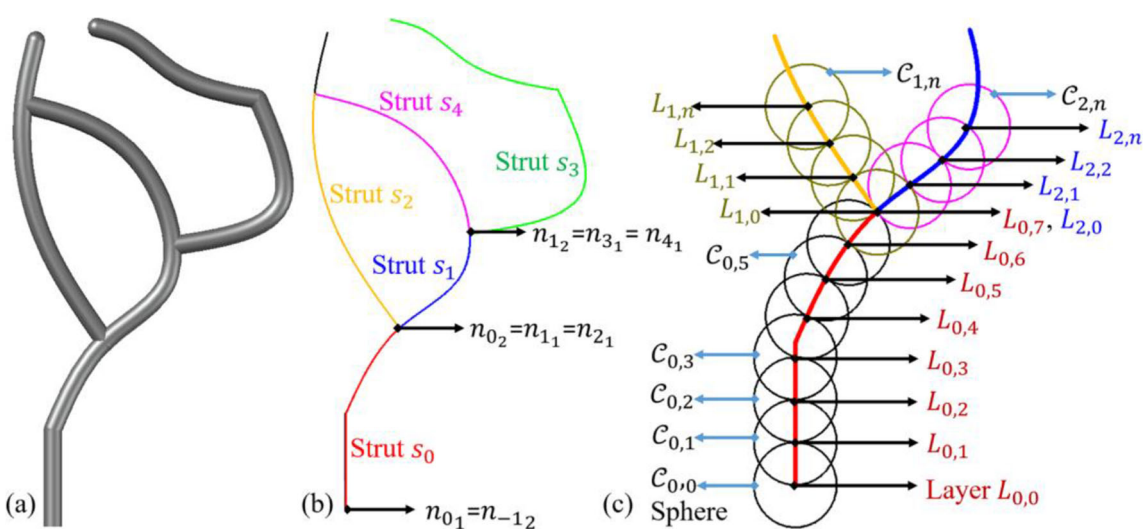


Fig. 8 Schematic diagrams of slicing methods. (a) Wire structure model, (b) acquisition of independent struts, (c) proposed strut slicing method

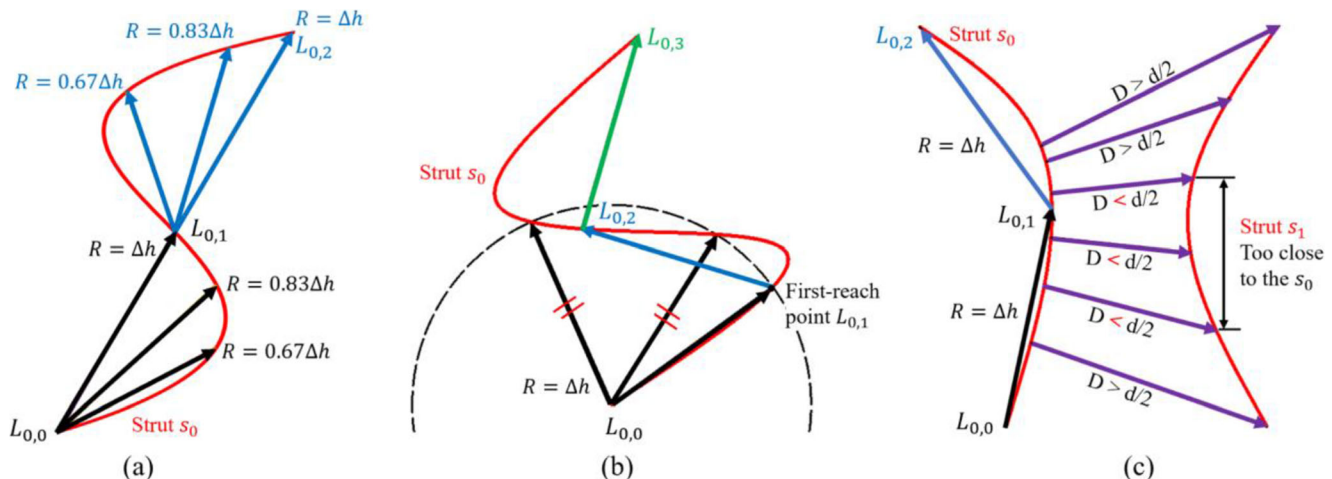


Fig. 9 The performance of the adaptive slicing for some build paths of struts. **(a)** changing a curve path with a large curvature into the straight line; **(b)** selecting the optimal point among multi-intersection points, and **(c)** comparing the mini-distance between struts for collision prediction

details may be lost due to the limitation of slicing accuracy. As shown in Fig. 9 (a), a curve path is represented by the polyline shaped like a straight line. When multiple points with a distance equal to Δh are found on the strut from a slice layer, as shown in Fig. 9 (b), the algorithm will select the first reach point along the build direction of the strut as the next slice layer to ensure that strut will not lose extra details.

The proposed algorithm also performs preliminary collision detection on struts with different end points, as shown in the example shown in Fig. 9 (c). For a strut, the lines with length $d/2$ are drawn along the vertical direction of its build direction. If some parts of another strut appear within this length, it means that the two struts are too close, and the depositing process will be blocked. It is noteworthy that there is no need to detect the collision of struts with the same end point, as they must have collision areas. The corresponding processing methods of them are shown in the next chapter.

The overall adaptive slicing method combined with the height control system is presented as a flow chart shown in Fig. 10. When there is a divergence between the actual deposition height of a layer and the theoretical height increment detected by the height control system, the method will regard this layer as the new start point to re-slice the remaining parts of the strut so as to ensure the stability of the entire depositing process. It is worth noting that the adjustment of the robot pose refers to the position of the tool center point (welding torch tip). Welding position and rotation are derived from the parts' coordinates and the building direction of each layer in the strut.

Combined with the height control system, the effectiveness of this adaptive slicing methodology is highlighted in Fig. 11, in which two arc-shaped struts are deposited with or without the present adaptive slicing method. Figure 11 (a) shows the strut fabricated successfully via the proposed adaptive method. While with a constant slicing height as shown in Fig. 11 (b) and (c), the positional errors in the static approach

accumulate as the deposition process continues, destroying the final geometric shape of the strut.

4.4 Handling branch intersection

The intersections of a wire structure occur where two or more struts' end points merge together, which is defined as a

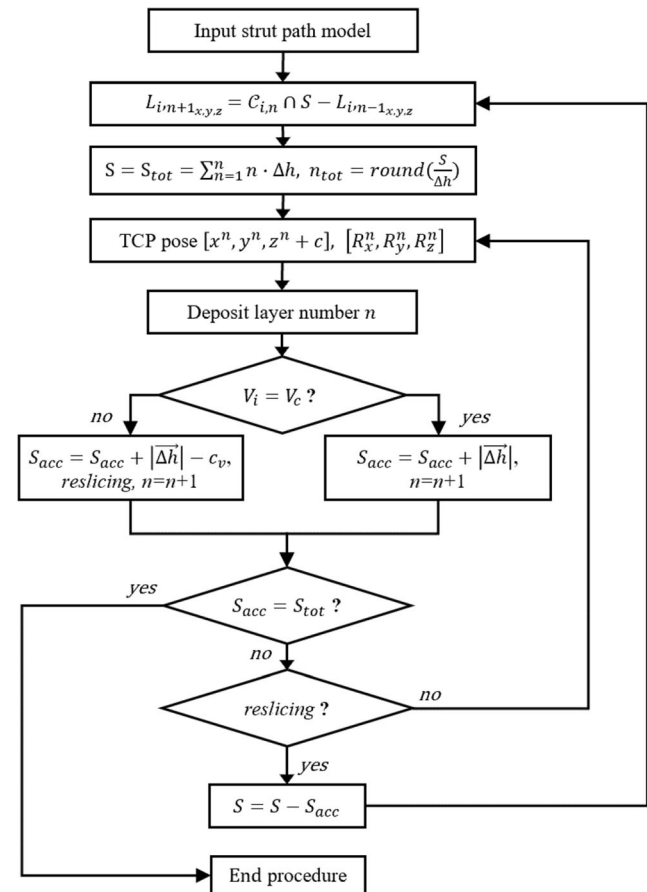
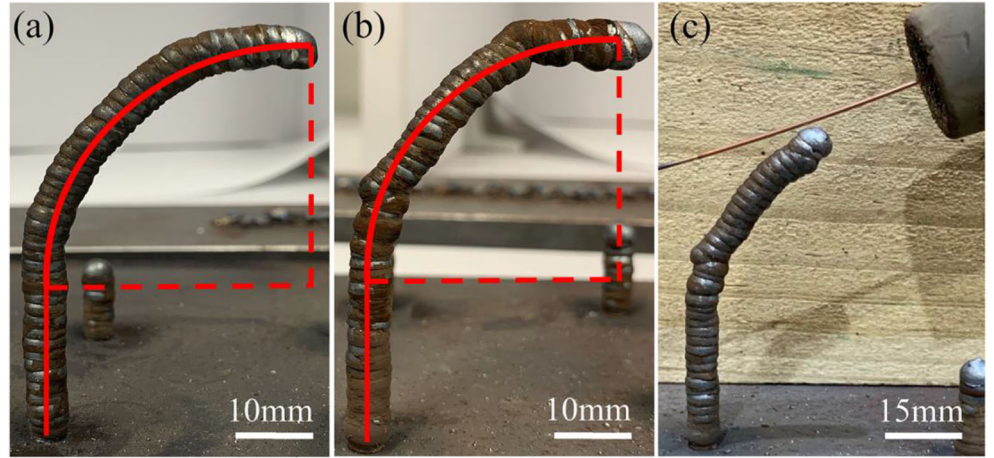


Fig. 10 Processes of the slicing and height control methods for the strut

Fig. 11 Arc-shaped strut deposition process (a) with adaptive CTWD changes, (b) in static deposition approach, (c) cumulative errors in (b) discontinue the deposition



convergent node; when the same end points of struts correspond to the start points of two or more new struts, then, it is called a divergent node, as shown in Fig. 12. As the deposition process for a given strut nears these nodes, some strategies need to be employed to avoid poor weld bead geometry or potential collision between the torch nozzle and the component.

For struts emanating from a divergent node, two build options are available. First, the struts could be deposited by alternating the deposition process evenly between them, so in effect, they are built up simultaneously. Alternatively, each strut can be deposited individually in one shot according to their strut number i , as shown in Fig. 12 (a). The first method usually produces poor strut geometry, as shown in Fig. 13 (a). This is mainly due to the slippage of the molten pool during the welding process. The molten pool is prone to be adsorbed towards the adjacent strut whose material has already been deposited so that the deposition process does not proceed in the expected position, resulting in a deformed structure. To avoid this phenomenon, struts at this point need to be continuously deposited and manufactured one-by-one according to

their corresponding processing sequence, as shown in Fig. 13 (b). Under this strategy, CTWD also needs to be dynamically adjusted to prevent the torch from collides with deposited struts if they have a small included angle, as shown in Fig. 13 (c).

4.5 Tool path planning strategy

The tool path planning strategy is then presented for processing a complete wire structure. The wire structure, which is expressed as $\mathcal{W} = \{\mathcal{S}, \mathcal{N}\}$, can be represented as intersection points set $\mathcal{N} = \{n_i | i = 1, 2, 3, \dots, |\mathcal{N}|\}$ and individual struts set $\mathcal{S} = \{s_i | i = 1, 2, 3, \dots, |\mathcal{S}|\}$. The first step in the path planning process is to identify struts that share the same convergent or divergent nodes. Any independent strut except for struts connected to the substrate must have a convergent node and a divergent node. Thus, for all struts $s_1, s_2, s_3, \dots, s_i = [n_{i_1}, n_{i_2}]$, these which have the same starting point are placed in the set $\mathcal{S}_{\mathcal{P}_m}^{div}$, defined as:

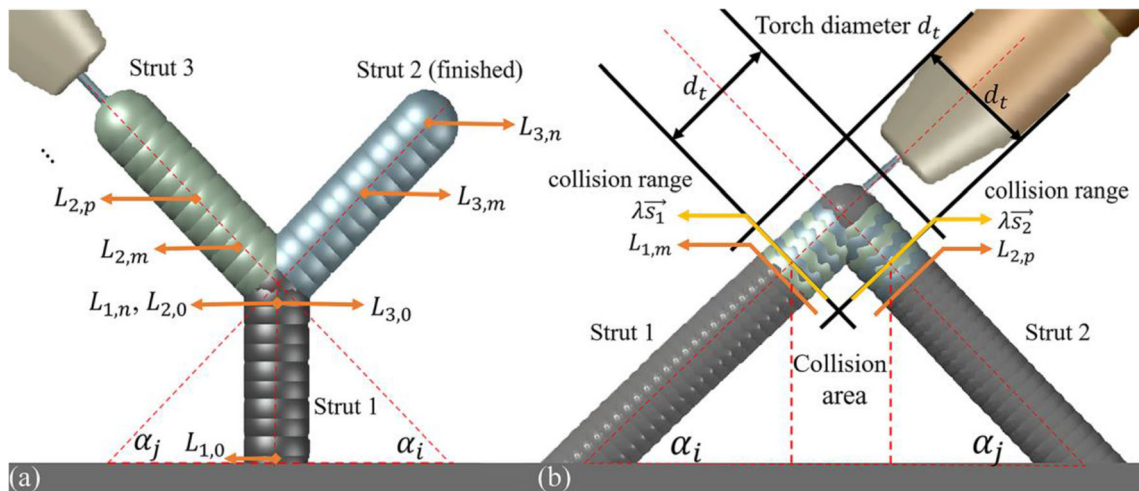


Fig. 12 The example of (a) the divergent node and (b) the convergent node

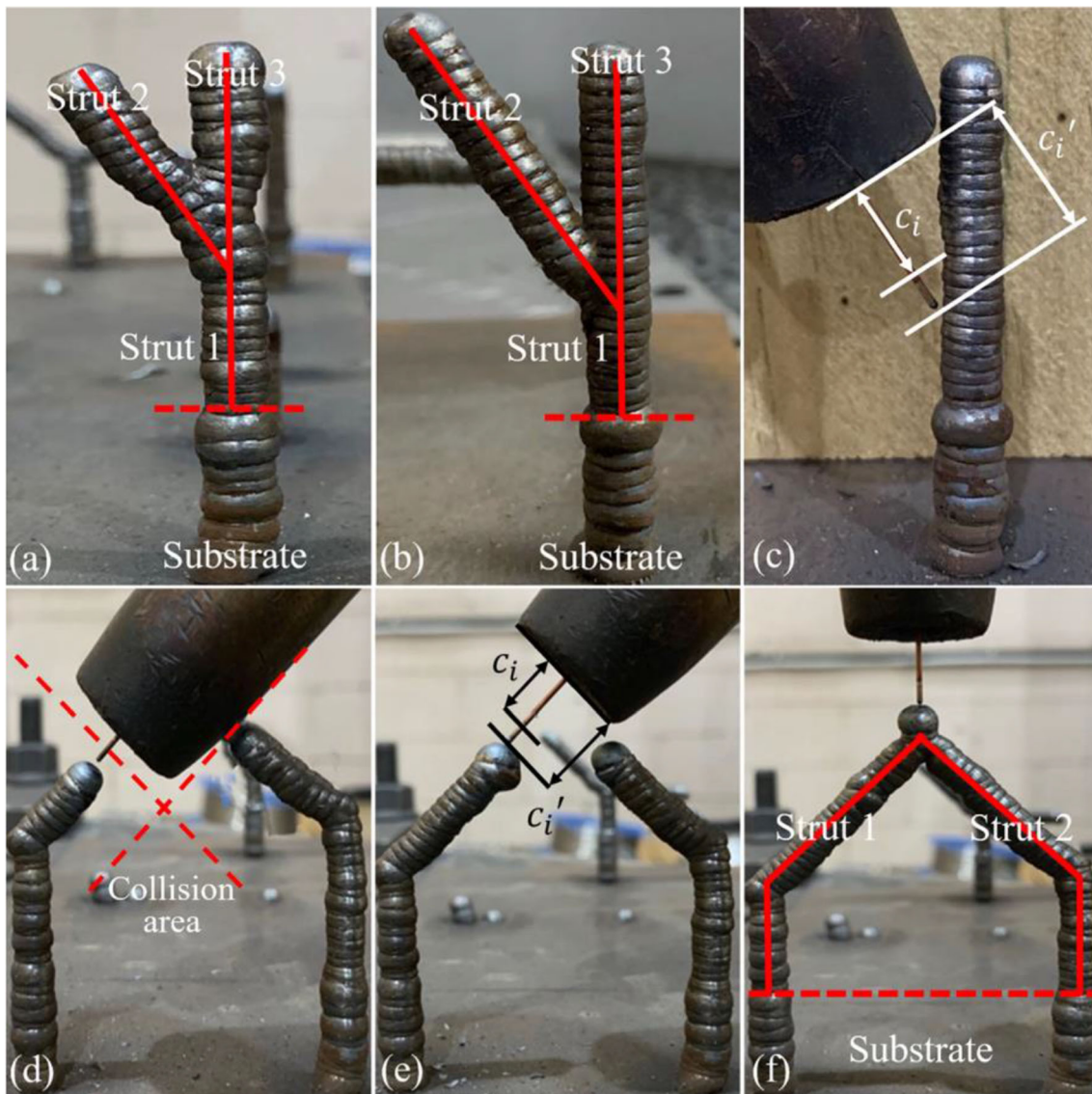


Fig. 13 Examples of fabricating branch intersections. For divergent samples: (a) deposit layer-by-layer in traditional z -direction; (b) deposit one-by-one in order; (c) adaptive CTWD changes to avoid collisions. For convergent nodes: (d) determine the collision area; (e) change CTWD to avoid collisions; (f) the final geometry of this sample

$$\begin{aligned} \mathcal{S}_{\mathcal{P}_m}^{div} &= \{s_i | n_{i1} = n_{j1}, i \in (1, |\mathcal{N}|), j \in (1, |\mathcal{N}|)\} \\ \mathcal{P}_m &= \{i | n_{i1} = n_{j1}, i \in (1, |\mathcal{N}|), j \in (1, |\mathcal{N}|)\} \end{aligned} \quad (9)$$

where

Therefore, all struts in \mathcal{S}^{div} that have the same start point is labelled as \mathcal{P}_m . Correspondingly, all struts which share the same particular end point are defined as:

$$\begin{aligned} \mathcal{S}_{\mathcal{P}_m}^{cov} &= \{s_i | n_{i2} = n_{j2}, i \in (1, |\mathcal{N}|), j \in (1, |\mathcal{N}|)\} \\ \mathcal{P}_m &= \{i | n_{i2} = n_{j2}, i \in (1, |\mathcal{N}|), j \in (1, |\mathcal{N}|)\} \end{aligned} \quad (10)$$

where

The build sequence of struts should be arranged in terms of their end point height (from low to high in the z -axis) to avoid a scenario where higher struts are processed blocking access

for the welding torch to deposit underneath struts. The next step is to generate a valid deposition sequence. As logic dictates, any given strut must have at least two additional struts underneath it to provide support (i.e., all struts will emanate from a node of two or more struts). This means that the end point of any strut will also be the starting point in another strut. With this in mind, struts that successfully deposited are put into the set $\mathcal{S}_k^p = \{s_k^p, \dots, s_k^p\}$. Struts that have not yet deposited or will be deposited soon are defined as:

$$\mathcal{S}_k^u = \mathcal{S} \setminus \mathcal{S}_k^p \quad (11)$$

When planning a deposition sequence, convergent nodes are used as the basis for the analysis. First, for a given convergent node, a search for all the struts which converge upon it

is performed. Then, all struts whose end points are consistent with their starting point expressed as:

where

$$\begin{aligned} & \cap_{s_i \in S_{\mathcal{P}_m}^{con}} (\mathcal{N}_{i1}, S_k^p) \neq \emptyset \quad \mathcal{N}_{i1} \\ & = \left\{ n_{j2} \mid n_{si1} = n_{sj2}, s_i \in S_{\mathcal{P}_m}^{cov}, s_j \in S \right\} \end{aligned} \quad (12)$$

The role of \mathcal{N}_{i1} is that for any strut in the set $S_{\mathcal{P}_m}^{con}$, it will index all other struts which share the same end point n_{j2} as its start point n_{i1} . This element is then compared one-by-one with each element in S_k^p . Only when S_k^p contains all the same elements as in \mathcal{N}_{i1} can a valid processing sequence be established. Figure 14 illustrates the overall geometric algorithm with a simple schematic model.

Since the length of stick out of the torch can be adjusted within a reasonable range, making its path planning more flexible, as stated by Yuan et al. [25], to achieve a collision-free deposition path, the $ctwd$ may need to be adjusted during the process. As mentioned previously, the struts in the set $S_{\mathcal{P}_m}^{cov}$ create a potential collision (between the torch and nearby struts) as the build nears a convergent node. If a strut s_i is treated as a vector, it has a higher probability of collision in the range $\lambda \vec{s}_i$, as shown in Fig. 12. The max collision area λ_{max} can be defined as:

$$\lambda_{max} = 1 - \max \left(\cup_{i=1, j=1}^n \frac{d_t |\vec{s}_i|}{\sqrt{|\vec{s}_i|^2 |\vec{s}_j|^2 - (\vec{s}_i \cdot \vec{s}_j)^2}} \right) \quad (13)$$

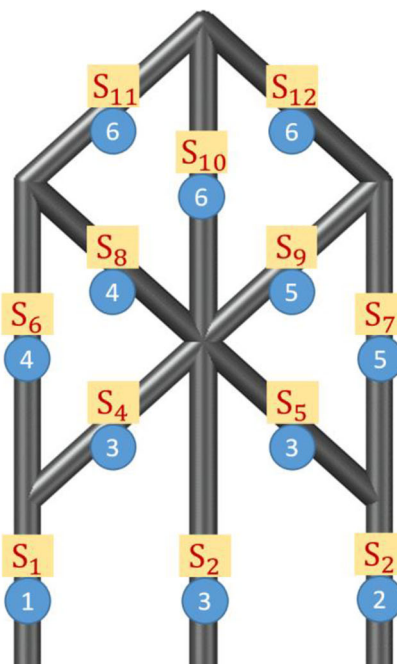


Fig. 14 An example of generating a deposition sequence for a wire structure

Struts must be compared one-by-one at this convergent point to determine the largest collision area. As the torch reaches the range of $(1 - \lambda_{max}) \vec{s}_i$, the $ctwd$ should be increased to ascertain the welding torch is outside the collision area, as shown in Fig. 13 (d) and (e). Similarly, when processing the strut near the divergence point, a collision check must be performed.

5 Case studies

To further verify the performance of the proposed strategy, two parts featuring complex wire structures were fabricated. In these two case studies, the same filler material, shielding gas, substrate material, automatic welding system, and all proposed fabrication strategy outlined in the previous section were used. The process parameters were maintained at $wfs = 4\text{m/min}$, $wt = 2\text{s}$ for all deposition processes.

5.1 The cube-shaped part fabrication process

Figure 14 shows the first fabricated part, a cube-shaped item defined by 12 struts, as shown in Fig. 15 (a). The length of all struts is about 30 mm, and the height of the main structure is about 52 mm. This structure has approximately 260 deposition layers and six intersection points, of which both the number of divergent nodes and convergent nodes are 3. It has five processing sequences, where struts 1, 2, and 3 have no convergent feature points, so they are regarded as one processing procedure. The final cube-shaped part is presented in Fig. 15 (c). The cool-down time between each layer of the welding

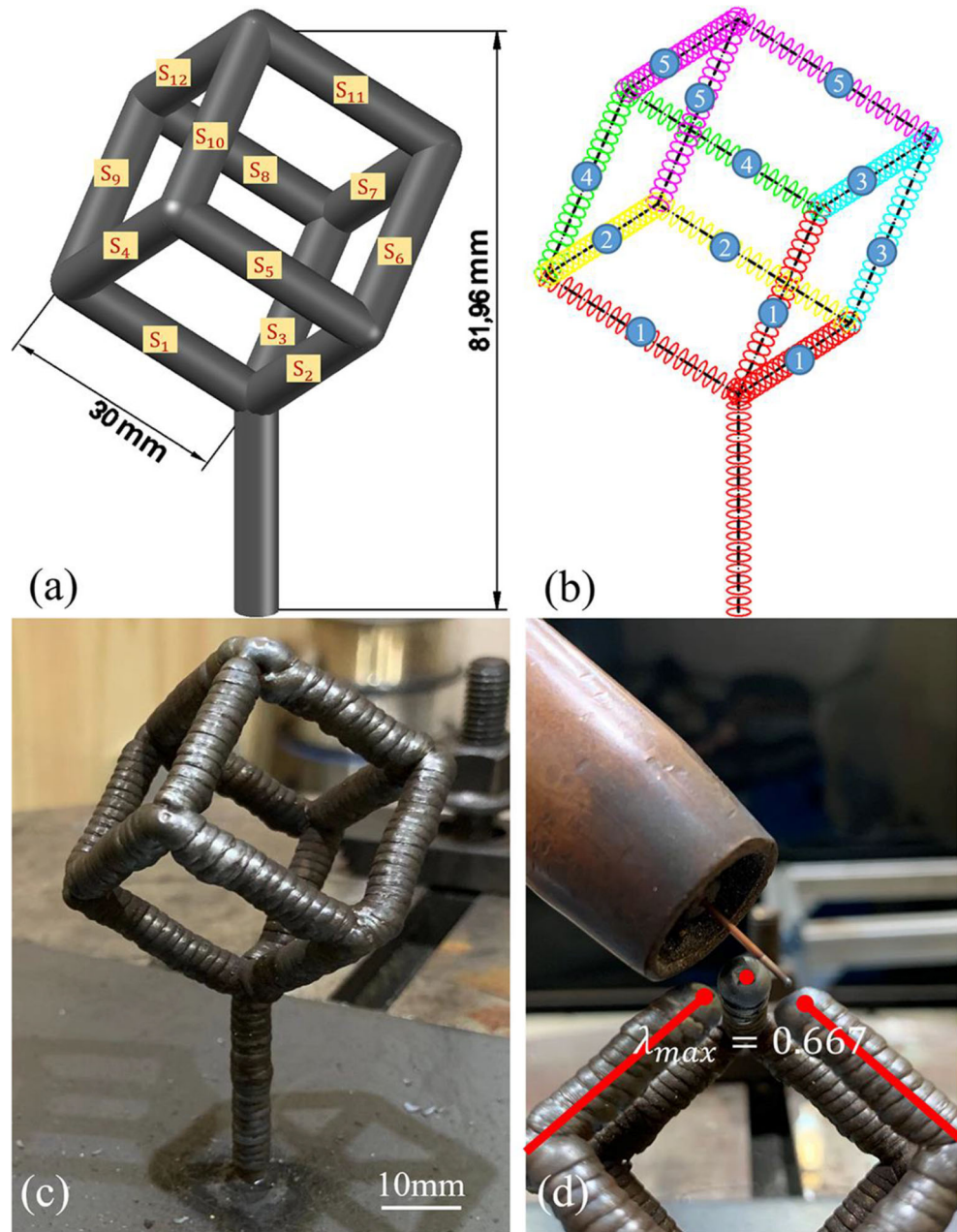
```

While  $\mathcal{S} \neq \emptyset$ :
    input candidate strut  $s_i$ 
     $S_{\{i\}}^{div} += s_i$  if  $n_{i1}$  in  $\mathcal{S}_{\{i\}}^{div}$  else create  $\mathcal{S}_{\{i\}}^{div}$ 
     $S_{\{i\}}^{cov} += s_i$  if  $n_{i1}$  in  $\mathcal{S}_{\{i\}}^{cov}$  else create  $\mathcal{S}_{\{i\}}^{cov}$ 
     $S_k^u += s_i$  pop from  $\mathcal{S}$ 

While  $S_k^u \neq \emptyset$ :
    input candidate strut  $s_i$ 
    if  $n_{i1}$  in  $S_k^p$ :
        find all  $\{s_j\}$ , where  $s_{j2} = s_{i2}$ 
        for  $n_{j1}$  in  $\{s_j\}$ :
            pass if  $n_{j1}$  in  $S_k^p$  else mark as unsupported; break
    if not unsupported:
        save all  $\{s_j\}$  as an independent sequence, into  $S_k^p$ 
         $S_k^u = \mathcal{S} \setminus S_k^p$ 
        call adaptive slicing algorithm
        call intersection processing strategy
        start deposition process

```

Fig. 15 Cube-shaped wire structure. (a) The STL model, (b) the slicing model, (c) the final part, and (d) a fabrication detail.



period was set to 30 s, and the total processing time of it was about 5 h. Figure 15 (d) illustrates some fabrication details of the layers near convergent nodes. Through the (13), the λ_{max} for all struts in the same convergent node is 0.667, which means that when the height of a strut in its build direction reaches about 20 mm, it is necessary to deposit all the struts in the same processing sequence layer-by-layer with their own layer number n .

5.2 Honeycomb-part fabrication process

Figure 16 shows the second fabricated part: A honeycomb-like part consisting of wire structures. Its main structure

contains a total of 24 struts. It has approximately 640 deposition layers with a total of 14 intersection points and a total of 12 processing sequences. The length of all struts is 30 mm. The height is about 150 mm, and the maximum width of it in the x -axis direction is about 156 mm. The final honeycomb-shaped part is presented in Fig. 16 (b). Its cool-down time between each layer of the welding period was also set to 30 s, and the total processing time of it was about 10 h. The collision range λ_{max} for all the struts is 0.6151. Therefore, when the height of the strut reaches about 18.45 mm, it is necessary to deposit them layer-by-layer.

Figure 16 (c) highlights a problem in the fabrication process. Due to the effect of heat accumulation, the cooling time

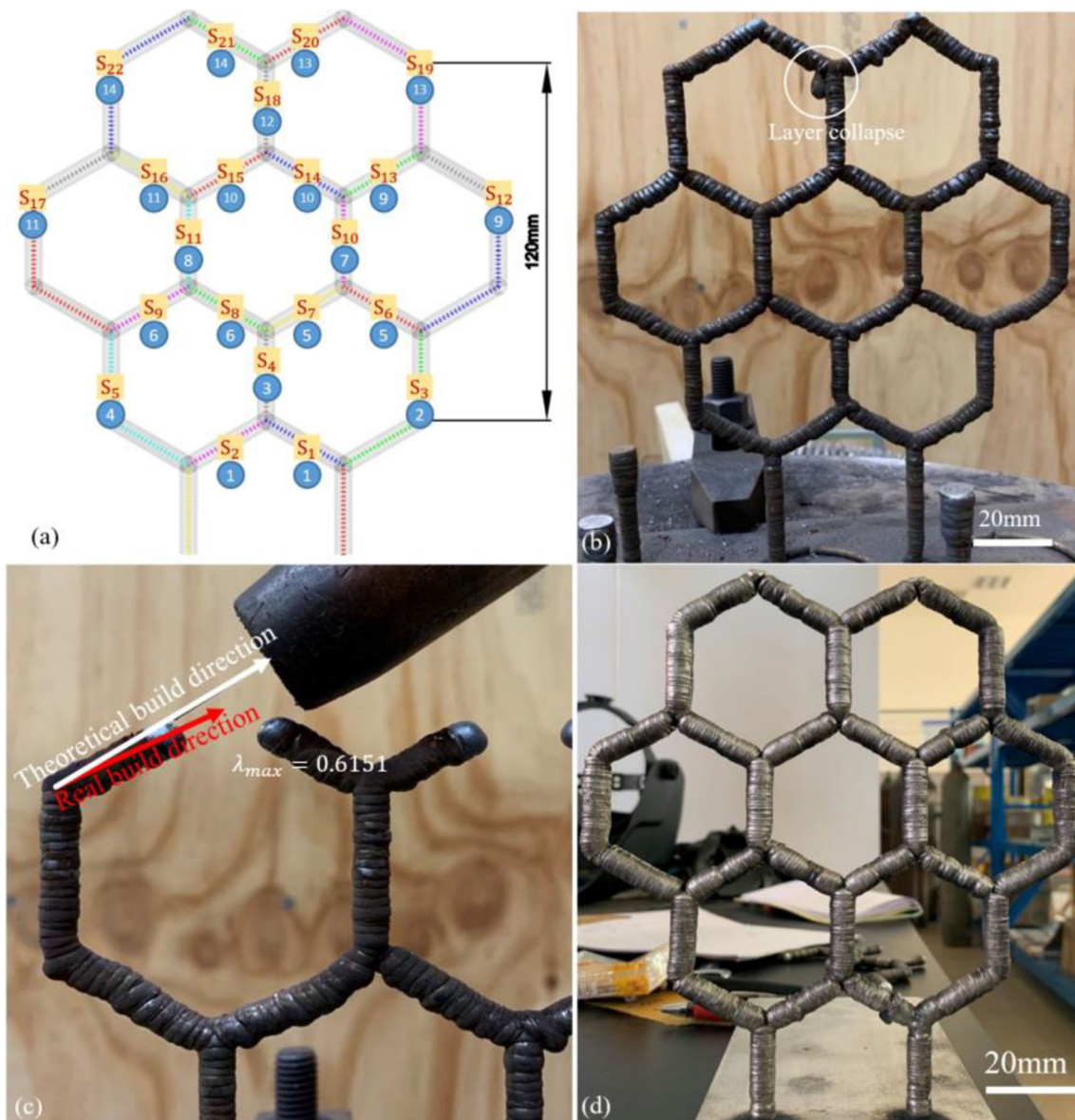


Fig. 16 Honeycomb-shaped wire structure. **(a)** The slicing model, **(b)** the part (mild steel), **(c)** the problem encountered in processing, and **(d)** the part (aluminum ER4043) with $v = 5$ m/min, $t = 1$ s, $d = 9$ mm, and $h = 1$ mm

of 30 s is not enough to cool it down to a suitable temperature range. The additional heat buildup affects the solidification process, and as a result, the build direction of the strut was observed to droop somewhat. This was not observed in the cube structure, as the inclined angles of the struts were less. In more severe cases, the deposit was observed to spill off the build layer before solidification. To address this, further experiments will make use of a temperature camera to monitor interpass temperatures of the welding process to adjust the cooling time dynamically. The influence of temperature on the strut can also be investigated in-depth via a detailed bead modelling study.

Moreover, the strategy proposed in the paper is robust and adaptive for almost all metal materials, as long as it can be

given stable welding parameters. As an extra example shown in Fig. 16 (d), this is the same honeycomb structure processed with aluminum ER4043 (bead modelling not explained here). In conclusion, the quality of the resultant geometry for these two steel parts and one aluminum part with the wire structure, particularly at intersection nodes, is good-looking and precise in position, highlighting the reliability and accuracy of the work proposed in this paper.

6 Conclusion

In this work, a WAAM strategy for fabricating components featuring wire structures via the point-by-point manner was

presented. Firstly, a bead modelling process was developed to accurately ascertain and predict the optimal process parameters for the desired bead geometry of the strut. Subsequently, the slicing algorithm and height control system were also presented to generate an adaptive slicing model. Then, these items are used in combination for the torch path planning of the overall deposition process. Finally, their effectiveness was demonstrated via the fabrication process of two separate parts featuring wire structure designs.

Further research aims to enhance the practicality of the proposed strategy and further develop the robotic system to deposit these wire structures reliably. The topology optimization process will be regarded as a research and development focus to split the entire workpiece into multiple independent regions, thereby reducing the time spent on processing workpieces with high space complexity. The work will also expand reliable and robust algorithms to reduce the weight of physical workpieces or convert them into stable skeleton structures and manufacturing arbitrary workpieces that combine wire structures and thin-walled structures and solid structures.

Author contribution All authors provided critical feedback and helped shape the research, analysis and manuscript.

Funding This work was supported in part by the National Natural Science Foundation of China under Grant 51805085, in part by the China Scholarship Council under Grant 201908200010.

Data Availability The datasets used or analyzed during the current study are available from the corresponding author on reasonable request.

Declarations

Ethics approval Authors promise that this manuscript is original, and it has not been published in whole or in part, nor is it being considered for publication or submission elsewhere.

Consent to participate We make sure the author group, the corresponding author, and the order of authors are all correct at submission.

Consent for publication The authors have reviewed the present version of the manuscript and approved it for publication.

Conflict of interest The authors declare no competing interests.

References

- Gibson I, Rosen D, Stucker B et al (2015) Directed energy deposition processes. *Addit Manuf Technol*:245–268. https://doi.org/10.1007/978-1-4939-2113-3_10
- Ding D, Pan Z, Cuiuri D, Li H (2015) Wire-feed additive manufacturing of metal components: technologies, developments and future interests. *Int J Adv Manuf Technol* 81:465–481. <https://doi.org/10.1007/s00170-015-7077-3>
- Williams SW, Martina F, Addison AC, Ding J, Pardal G, Colegrove P (2016) Wire + Arc additive manufacturing. *Mater Sci Technol (United Kingdom)* 32:641–647. <https://doi.org/10.1179/1743284715Y.0000000073>
- Shen C, Pan Z, Ding D, Yuan L, Nie N, Wang Y, Luo D, Cuiuri D, van Duin S, Li H (2018) The influence of post-production heat treatment on the multi-directional properties of nickel-aluminum bronze alloy fabricated using wire-arc additive manufacturing process. *Addit Manuf* 23:411–421. <https://doi.org/10.1016/j.addma.2018.08.008>
- Yilmaz O, Ugla AA (2016) Shaped metal deposition technique in additive manufacturing: a review. *Proc Inst Mech Eng Part B Eng Manuf* 230:1781–1798. <https://doi.org/10.1177/0954405416640181>
- Guo N, Leu MC (2013) Additive manufacturing: technology, applications and research needs. *Front Mech Eng* 8:215–243. <https://doi.org/10.1007/s11465-013-0248-8>
- Kloft H, Empelmann M, Hack N, Herrmann E, Lowke D (2020) Reinforcement strategies for 3D-concrete-printing. *Civ Eng Des* 2: 131–139. <https://doi.org/10.1002/cend.202000022>
- Gardner L, Kyvelou P, Herbert G, Buchanan C (2020) Testing and initial verification of the world's first metal 3D printed bridge. *J Constr Steel Res* 172:172–106233. <https://doi.org/10.1016/j.jcsr.2020.106233>
- Laghi V, Palermo M, Gasparini G, Veljkovic M, Trombetti T (2020) Assessment of design mechanical parameters and partial safety factors for wire-and-arc additive manufactured stainless steel. *Eng Struct* 225:111314. <https://doi.org/10.1016/j.engstruct.2020.111314>
- Ngo TD, Kashani A, Imbalzano G, Nguyen KTQ, Hui D (2018) Additive manufacturing (3D printing): a review of materials, methods, applications and challenges. *Compos Part B Eng* 143: 172–196. <https://doi.org/10.1016/j.compositesb.2018.02.012>
- Radel S, Diourte A, Soulié F, Company O, Bordreuil C (2019) Skeleton arc additive manufacturing with closed loop control. *Addit Manuf* 26:106–116. <https://doi.org/10.1016/j.addma.2019.01.003>
- Huang Y, Zhang J, Hu X et al (2016) FrameFab : robotic fabrication of frame shapes. 35:1–11
- Mueller S, Im S, Gurevich S et al (2014) WirePrint: fast 3D printed previews. *Proc UIST*:273–280
- Li Y, Yu S, Chen Y, Yu R, Shi Y (2020) Wire and arc additive manufacturing of aluminum alloy lattice structure. *J Manuf Process* 50:510–519. <https://doi.org/10.1016/j.jmapro.2019.12.049>
- Laghi V, Palermo M, Gasparini G, Trombetti T (2020) Computational design and manufacturing of a half-scaled 3D-printed stainless steel diagrid column. *Addit Manuf* 36:101505. <https://doi.org/10.1016/j.addma.2020.101505>
- Wu B, Pan Z, Ding D, Cuiuri D, Li H, Xu J, Norrish J (2018) A review of the wire arc additive manufacturing of metals: properties, defects and quality improvement. *J Manuf Process* 35:127–139. <https://doi.org/10.1016/j.jmapro.2018.08.001>
- Ding D, Shen C, Pan Z, Cuiuri D, Li H, Larkin N, van Duin S (2016) Towards an automated robotic arc-welding-based additive manufacturing system from CAD to finished part. *CAD Comput Aided Des* 73:66–75. <https://doi.org/10.1016/j.cad.2015.12.003>
- Yuan L, Ding D, Pan Z, Yu Z, Wu B, van Duin S, Li H, Li W (2020) Application of multi-directional robotic wire arc additive manufacturing process for the fabrication of complex metallic parts. *IEEE Trans Ind Informatics* 16:1–1. <https://doi.org/10.1109/tii.2019.2935233> 464
- Xu J, Gu X, Ding D, Pan Z, Chen K (2018) A review of slicing methods for directed energy deposition based additive manufacturing. *Rapid Prototyp J* 24:1012–1025

20. Wu R, Peng H, Guimbretière F, Marschner S (2016) Printing arbitrary meshes with a 5DOF wireframe printer. ACM Trans Graph 35:1–9. <https://doi.org/10.1145/2897824.2925966>
21. Müller J, Grabowski M, Müller C, Hensel J, Unglaub J, Thiele K, Kloft H, Dilger K (2019) Design and parameter identification of wire and arc additively manufactured (WAAM) steel bars for use in construction. Metals (Basel) 9. <https://doi.org/10.3390/met9070725>
22. Abe T, Sasahara H (2019) Layer geometry control for the fabrication of lattice structures by wire and arc additive manufacturing. Addit Manuf 28:639–648. <https://doi.org/10.1016/j.addma.2019.06.010>
23. Ding D, Pan Z, Cuiuri D, Li H (2015) A practical path planning methodology for wire and arc additive manufacturing of thin-walled structures. Robot Comput Integr Manuf 34:8–19. <https://doi.org/10.1016/j.rcim.2015.01.003>
24. Luo Y, Li J, Xu J et al (2018) The CMT short-circuiting metal transfer process and its use in thin aluminium sheets welding. Mater Des 30:1850–1852. <https://doi.org/10.1016/j.matdes.2008.07.015>
25. Yuan L, Pan Z, Ding D, Yu Z, van Duin S, Li H, Li W, Norrish J (2020) Fabrication of metallic parts with overhanging structures using the robotic wire arc additive manufacturing. J Manuf Process 63:0–1. <https://doi.org/10.1016/j.jmapro.2020.03.018> 24

Publisher's note Springer Nature remains neutral with regard to jurisdictional claims in published maps and institutional affiliations.